Ultra-effective integrated technologies for water disinfection with a novel 0D-2D-3D nanostructured rGO-AgNP/$Bi_2Fe_4O_9$ composite

Zhong-Ting Hu[a,b,*], Yen Nan Liang[c,d], Jun Zhao[e], Yingdan Zhang[f], En-Hua Yang[b], Jianmeng Chen[a], Teik-Thye Lim[b,d,**]

[a] College of Environment, Zhejiang University of Technology, Hangzhou 310014, China
[b] School of Civil and Environmental Engineering, Nanyang Technological University (NTU), Singapore 639798, Singapore
[c] School of Material Science and Engineering, NTU, Singapore, Singapore
[d] Environmental Chemistry & Materials Centre, Nanyang Environment and Water Research Institute, NTU, Singapore, Singapore
[e] School of Chemical and Biomedical Engineering, NTU, Singapore, Singapore
[f] Singapore Center on Environmental Life Sciences Engineering, NTU, Singapore, Singapore

ARTICLE INFO

ABSTRACT

Emerging technologies for water disinfection is being developed to reduce waterborne disease efficiently. Herein, we report a novel bactericidal technology incorporating 0D-2D-3D nanostructured rGO-Ag/$Bi_2Fe_4O_9$ (BFOA-G) composites which exhibited ultra-effective disinfection efficacies towards Gram-negative *E. coli* and *P. aeruginosa*, and Gram-positive *S. aureus*. Owing to the synergistic action among BFO ($Bi_2Fe_4O_9$), AgNPs (Ag nanoparticles) and rGO (reduced graphene oxide) within BFOA-G, the H_2O_2/Vis/BFOA-G system (Vis, $420 < \lambda < 630$ nm) showed remarkable bactericidal performance of approaching 100% efficacy (≥ 6 logs) of *E. coli* in 20 min with the inhibition of Ag^+ leaching (usually achieving 3 logs of bacterial reduction around 1–4 h in photocatalytic disinfection). This system is defined as "integrated technology" that involves varied disinfection processes/mechanisms of rGO-assisted Ag^+ release, Ag-assisted Fenton reaction, Ag/rGO co-assisted photocatalysis and Ag-assisted photo-Fenton oxidation. This novel BFOA-G was produced by incorporating the *in-situ* synthesized 0D-3D Ag-BFO (AgNP size of 5–20 nm) with 2D rGO *via* a facile evaporation process at 75 °C. The bacterial cell membrane damage caused by reactive oxygen species (ROSs) was verified by staining the cells using Live/Dead Baclight Kit. This study provides new insights into potential of nanostructured composites for developing innovative water disinfection technologies.

1. Introduction

According to World Health Organization (WHO) (2015), there are over half a billion people who lack access to safe drinking water and millions of mortalities due to waterborne pathogens [1]. Although traditional technologies (*e.g.*, ozonation, chlorination, and UV radiation) can inactivate many pathogenic microbes, they are limited by their formation of harmful disinfection by-products (DBPs), high energy consumption or environmental hazards (*e.g.*, Hg) [2,3]. Moreover, tolerant pathogens undergoing stimulation, evolution and variation are gradually emerging resulting from the aggravation of environmental contamination [4]. Hence, a novel water disinfection technology that is versatile, robust, environment-friendly, cost-effective and energy-efficient is overdue.

Water disinfection technology based on zero-dimensional (0D)

AgNPs is gaining a great deal of attention, which is attributed to its excellent antimicrobial action and other unique physicochemical properties such as surface plasmon resonance (SPR) and electron conductivity [5–7]. The bactericidal mechanism of AgNPs mainly involves (1) the damage of cell membranes *via* the conversion of Ag^0/Ag^+ with formation of ROSs, and (2) interruption of intracellular metabolic pathways due to Ag^+ penetration into the cells causing adverse effects (*e.g.*, inhibiting adenosine triphosphate formation and enzymes activity) [8–10]. However, environmental toxicity of AgNPs has been attracting attention in the past several years since AgNPs are dispersible with Ag^+ release [11,12]. One of the most effective strategies to address metal leaching from nanoparticles is to fabricate composites [13,14]. For example, Loo et al. fabricated a cryogel decorated with AgNPs and applied it to develop a novel absorb-squeeze strategy for water disinfection with a low-level Ag leaching [13].

Catalytic technologies (especially for heterogeneous catalysis), such as photocatalysis (formation of $O_2 \cdot^-$, $HO \cdot$) and Fenton-like reaction (H_2O_2 converted to $HO \cdot$ or $HO_2 \cdot$), have great potential for water disinfection [15,16]. The generated ROSs can induce irreparably oxidative damage to DNA, proteins and cell membranes for pathogens [17,18]. Up to now, many types of catalysts with varied bandgaps have been developed and employed for photocatalytic disinfection including typically UV-excited TiO_2 or ZnO (~ 3.2 eV) [15], and Vis-excited WO_3 (2.4–2.8 eV) or MoS_2 (1.3–1.9 eV) [16,19]. Nevertheless, the free metal ions, which formed on the surface of catalyst, are possibly hazardous to the ecosystem. Among them, TiO_2 has great potential for water disinfection because of its low-toxicity, chemical stability and strong oxidizing ability, but certain disadvantages, *e.g.*, high recombination of electron-hole (e^-/h^+) pairs and large bandgaps, limit its widespread usage [20]. Composite usually exhibits synergistic effects by combining the properties of component phases. It can be a robust catalyst with both remarkable performances and multi-dimensional structures (*i.e.*, 0D, 1D, 2D, 3D). Two-phase composites as catalysts have attracted considerable attention for water disinfection, namely TiO_2-Bi_2WO_6, TiO_2-Fe_3O_4, Ag-TiO_2, Ag-SiO_2, Ag-AgX (X is Br, Cl, I), Fe-clay, Au-TiO_2, Cd-TiO_2, ZnO-TiO_2, WO_3-TiO_2, and $NaNbO_3$-WO_3 [14,15,21–23]. In general, disinfection time in the photocatalytic disinfection from 1 to 4 h is required for over 3 logs of bacterial inactivation [15].

Graphene is a fascinating nanocarbon possessing 2D layered structure with unique characteristics including large specific surface area, three types of adsorption sites (*i.e.*, hollow, bridge and midpoint sites) and superior electron mobility [24]. Recently, graphene oxide (GO) has been used as a catalyst support to design three-phase composites such as 0D-2D-2D nanostructured GO-MoS_2/TiO_2, 0D-0D-2D GO-Cu/TiO_2, 0D-1D-2D rGO-WO_3/TiO_2 and 0D-2D-2D rGO-gC_3N_4/TiO_2 [25–27]. We also reported a novel 0D-2D-3D rGO-Ag/$Bi_2Fe_4O_9$ composite for enhanced environmental decontamination of organic pollutants, wherein the individual functions of the components (*e.g.*, multiple catalyses of BFO, Ag-assisted redox conversion of Fe^{3+}/Fe^{2+} pair, antirecombination of e^-/h^+ pairs of rGO) in nanocomposite were demonstrated [28]. Herein, an ultra-efficient "integrated technology" for water disinfection based on BFOA-G is reported for the first time. The performances in bacterial inactivation for Gram-negative and Gram-positive bacteria were systematically studied. The results revealed that BFOA-G based systems show remarkable/enhanced bactericidal performance with the inhibition of Ag^+ leaching. The integrity of the bacterial cell membranes was evaluated by staining the cells using Live/Dead Baclight Kit. The bactericidal mechanisms integrating varied pathways in H_2O_2/Vis/ BFOA-G system are well investigated according to comparative experiments associated with material characterization and chemical analysis.

2. Materials and methods

2.1. Chemicals and materials

All the chemicals were used in this study as received without further purification. Potassium permanganate (99%), urea (99%), concentrated sulfuric acid (98%), sodium nitrate (99%), (3-aminopropyl)-trimethoxysilane (ATPES, > 98%), glutaraldehyde (GA, 25%), silver nitrate (99%), and methylene blue (95%) were purchased from Sigma-Aldrich. Potassium chloride (> 99%), sodium chloride (> 99%), ferric (III) nitrate nonahydrate (> 99%), nitric acid (1N), citric acid (> 99%), sodium dihydrogen phosphate monohydrate (> 98%), ammonia solution (25%), and methanol (LC grade) were purchased from Merck. Natural graphite powder with 325 mesh (> 99.9%), monopotassium phosphate (> 99%), hydrogen peroxide (35% by w/w), and sodium borohydride (98%) were purchased from Alfa Aesar. Other chemicals include sodium phosphate dibasic (> 99%, Asia Pacific Specialty Chemicals), bismuth (III) nitrate pentahydrate (> 98%, VWR), sodium hydroxide (pellet, Schedelco), and absolute ethanol (99.9%, Fisher

chemical). Milli-Q ultrapure water (18.2 MΩ cm) was used for all the experiments.

2.2. Bacterial strains

Model bacteria selected are Gram-negative *Escherichia coli* FDA strain Seattle 1946 (ATCC25922) and *Pseudomonas aeruginosa* Boston 41501 (ATCC27853), and Gram-positive *Staphylococcus aureus* FDA 209 (ATCC6538) in this study. All bacterial strains were routinely maintained in Luria-Bertani (LB) medium with 25% glycerol at $-80\,^\circ$C.

2.3. Preparation of nanocomposites

The detailed procedures of material preparations are presented in the Supporting information. Bismuth ferrite (BFO) with a 3D cuboid-like shape was prepared by combining low-temperature co-precipitation and hydrothermal treatment in a co-solvent system [29]. One-layered 2D graphene oxide (GO) was pre-prepared by a modified Hummers method [30,31]. By introducing a certain amount of $NaBH_4$ as reducing agent, GO was controllably converted into partially reduced GO (rGO) under ultrasonication [28]. 0D-3D nanostructured AgNP-decorated BFO composite was prepared by a multistep synthesis method sequentially undergoing surface modification (*i.e.*, amino- and aldehyde- functionalization) and AgNPs decoration (*in-situ* crystallization of adsorbed $[Ag(NH_3)_2]^+$) on the surface of BFO [28]. The as-prepared samples were denoted as BFOA1 and BFOA5 with addition of 10 mg and 50 mg of $AgNO_3$, respectively. The final product was washed and then dried in a vacuum oven at 65 °C overnight followed by calcination at 250 °C for 1 h under a N_2 atmosphere to remove residual solvents and organic compounds. 0D-2D-3D rGO-Ag/BFO nanocomposite was fabricated using a facile evaporation process at 75 °C after mixing BFOA1 ethanol and rGO water dispersions [28]. Thereafter, the post-treatment processes were similar with BFOA1 preparation. The final product was denoted as BFOA1-G.

2.4. Characterization

The as-prepared samples were characterized and differentiated by different characterization techniques. The morphology and nanostructure were investigated using field emission scanning electron microscopy (FESEM, JEOL JSM-7600F) and transmission electron microscopy (TEM, JEOL JEM-2010). The crystal phase was studied by powder X-ray diffraction (XRD) analysis (Bruker, D8 Advance, Cu Kα; λ = 1.5418 Å). The chemical composition and elemental distribution were examined by X-ray photoelectron spectroscopy (XPS, Kratos Axis Ultra Spectrometer, Al Kα at 1486.7 eV, 15 kV voltage, 10 mA emission current) and energy dispersive X-ray (EDX, Oxford Xmax80 LN2 Free) microanalysis. The materials were further characterized using Fourier transform-infrared spectroscopy (FT-IR, PerkinElmer GX), UV–vis diffuse reflectance spectroscopy (DRS, UV-2600, Shimadzu), thermogravimetric analysis (TGA, PerkinElmer, TGA-4000) with a ramp rate of $10\,^\circ$C min^{-1} under dry air, and photoluminescence (PL) emission spectroscopy (PerkinElmer, LS55).

2.5. Bactericidal activity test

Gram-negative (*i.e.*, *E. coli* and *P. aeruginosa*) and Gram-positive (*i.e.*, *S. aureus*) bacteria were selected as the model pathogens for the bactericidal activity test. Aliquots of frozen stock of bacteria (*e.g.*, *E. coli*) were inoculated on a Tryptone Soya Agar (TSA, Oxoid) plate and incubated at 37 °C for 24 h in an incubator oven (Memmert, Germany). After that, single colony of *E. coli* was inoculated into 20 ml LB broth and cultivated in a shaking incubator (150 rpm, Excella E24 Incubator Shaker Series, New Brunswick Scientific) at 37 °C for 18 h. The bacterial cells were harvested by centrifuging and washed with phosphate-buffered saline (PBS, 0.01 M, pH 7.4) solution followed by resuspension in
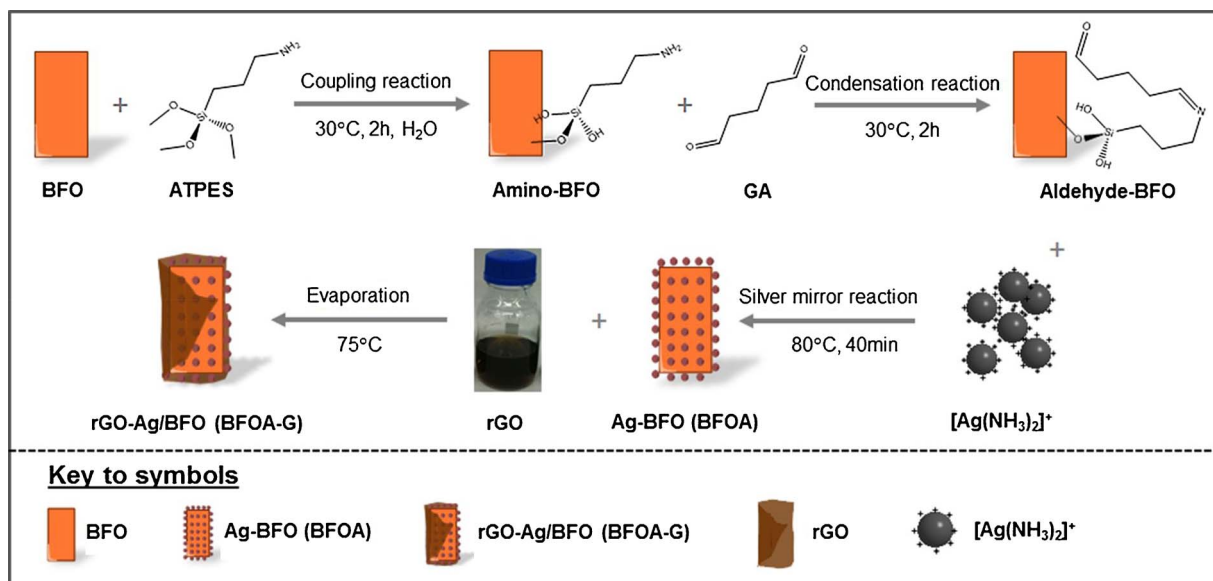
Fig. 1. Illustrative procedure for synthesis of 0D-3D Ag-BFO (BFOA) and 0D-2D-3D rGO-Ag/BFO (BFOA-G) nanocomposites.

PBS with cell density at 10^8 colony forming units per mL (cfu mL^{-1}).

Disinfection experiments were carried in the following four conditions: (1) dark without H_2O_2 (namely dark/material system, (2) dark with H_2O_2 (namely H_2O_2/material system), (3) under visible light (420 nm < λ < 630 nm) without H_2O_2 (namely Vis/material system), and (4) under visible light with H_2O_2 (namely H_2O_2/Vis/material system). Influence of key factors such as dosage of H_2O_2 (0–250 mg L^{-1}), nanomaterial loading (0–0.5 g L^{-1}), and types of nanomaterials (e.g., BFO, BFOA1, BFOA5, or BFOA1-G) on disinfection in each condition were investigated. Consistently, 10 ml PBS suspension containing E. coli ($\sim 10^6$ cfu mL^{-1}) in the absence or presence of nanomaterials (0.1 g L^{-1}) was stirred and maintained at room temperature in a water bath. At each designated time interval, 0.5 ml of the E. coli solution was drawn and diluted in PBS solution. After appropriate dilution, 0.1 ml of the diluted sample was spread on agar plate followed by incubation at 37 °C for 24 h. The colonies were counted to determine the number of viable bacteria. At least three replicate experiments were conducted. All experiments were carried out in biological safety cabinets (BSC, NuAire, Nu-440-400E). All the consumables used in the experiments were sterilized at 121 °C for 15 min in an autoclave (Hirayama HG-50, Japan) or under UV radiation (254 nm) for 20 min. The Ag$^+$ leaching after 60 min from the as-prepared nanomaterials in different experimental systems was quantified individually using inductively coupled plasma-mass spectrometry (ICP-MS, Perkin Elmer Elan DRC-e).

Live/Dead BacLight Bacterial Viability Kit (L7007, Molecular Probes) as a two-color fluorescence assay can be a reliable and quantitative approach to evaluate the integrity of the bacterial cell membranes (more information is described in Supporting information) [32]. 10 ml reaction in PBS with $\sim 10^6$ cfu mL^{-1} was centrifuged and resuspended into NaCl solution (0.85%) with an appropriate cell density. Control and treated samples were mixed with equal volumes of dye components A and B mixture for 15 min in the dark. After that, cell suspension was placed between a glass microscope slide and cover slip. Stained samples were observed using an epifluorescence microscope (Olympus BX60) equipped a 100× oil objective at the 470 nm excitation wavelength (notes: emission wavelengths for PI and SYTO 9 are at 630 and 530 nm, respectively).

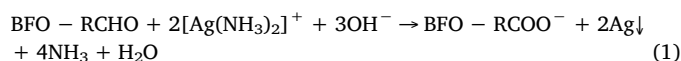### 2.6. Visible-light-driven catalytic activity test

Methylene blue (MB) was used as the model pollutant for evaluation

of catalytic activities of the as-prepared nanomaterials including BFO, BFOA1 and BFOA1-G. As described in our previous work [28], experiments were conducted in a reactor equipped with a solar simulator (Newport, 150 W xenon arc lamp, 1 sun) under the control of visible light region (420 nm < λ < 630 nm). The desired amount of the as-prepared nanomaterial (0.12 g L^{-1}) was added into 50 ml MB solution (5 mg L^{-1}) followed by continuous stirring for 1 h in the dark to achieve adsorption/desorption equilibrium. Before excitation of catalytic activities under visible light irradiation, the suspension was added with or without 1 mmol of H_2O_2 (20 mM, namely 680 mg L^{-1}) for the Fenton-like reaction and photocatalysis, respectively. A certain amount of solution was drawn out from the reaction vessel at the designated time interval. After the catalysts were separated by centrifugation, the supernatant solutions were analyzed by UV–vis absorption with an UV–vis spectrometer (UV-1800, Shimadzu).

3. Results and discussion

3.1. Synthesis and characterization of nanocomposites

In-situ synthesis of 0D-3D Ag-BFO (BFOA) nanocomposite under mild conditions involves (1) adsorption of formed [Ag(NH$_3$)$_2$]$^+$ ions with surface-modified BFO followed by (2) crystallization of AgNPs via silver mirror reaction as shown below (Reaction (1)). The 0D-2D-3D rGO-Ag/BFO (BFOA-G) nanocomposite was sequentially synthesized by a facile evaporation process at 75 °C (Fig. 1).

$$BFO - RCHO + 2[Ag(NH_3)_2]^+ + 3OH^- \rightarrow BFO - RCOO^- + 2Ag\downarrow + 4NH_3 + H_2O \qquad (1)$$

The morphology of BFOA1 is shown in Fig. 2a, with the corresponding EDX elemental distribution mappings of Bi, Fe and Ag in Fig. 2(a1–a3). The morphology of BFOA1 is consistent with BFO (Fig. S1a) which is of a cuboid-like shape with a side length of ~ 230 nm and a height of ~ 600 nm. The elemental distribution of Ag (Fig. 2a3) within the as-prepared BFOA1 is uniform which is ascribed to the in-situ synthesis method adopted. This suggests that the AgNPs have been well decorated on the surface of BFO. As shown in Fig. 2b, TEM images show that AgNPs with particle size of 5–20 nm (Fig. 2b1) are homogeneously anchored on BFO and it displays lattice fringes with d-spacing of 0.24 nm corresponding to the major crystal plane (111) [33]. For BFOA5, an increase in the addition of AgNO$_3$ in experiments led to an increase in the AgNPs deposition on the surface of BFO (Fig. S1b and c).
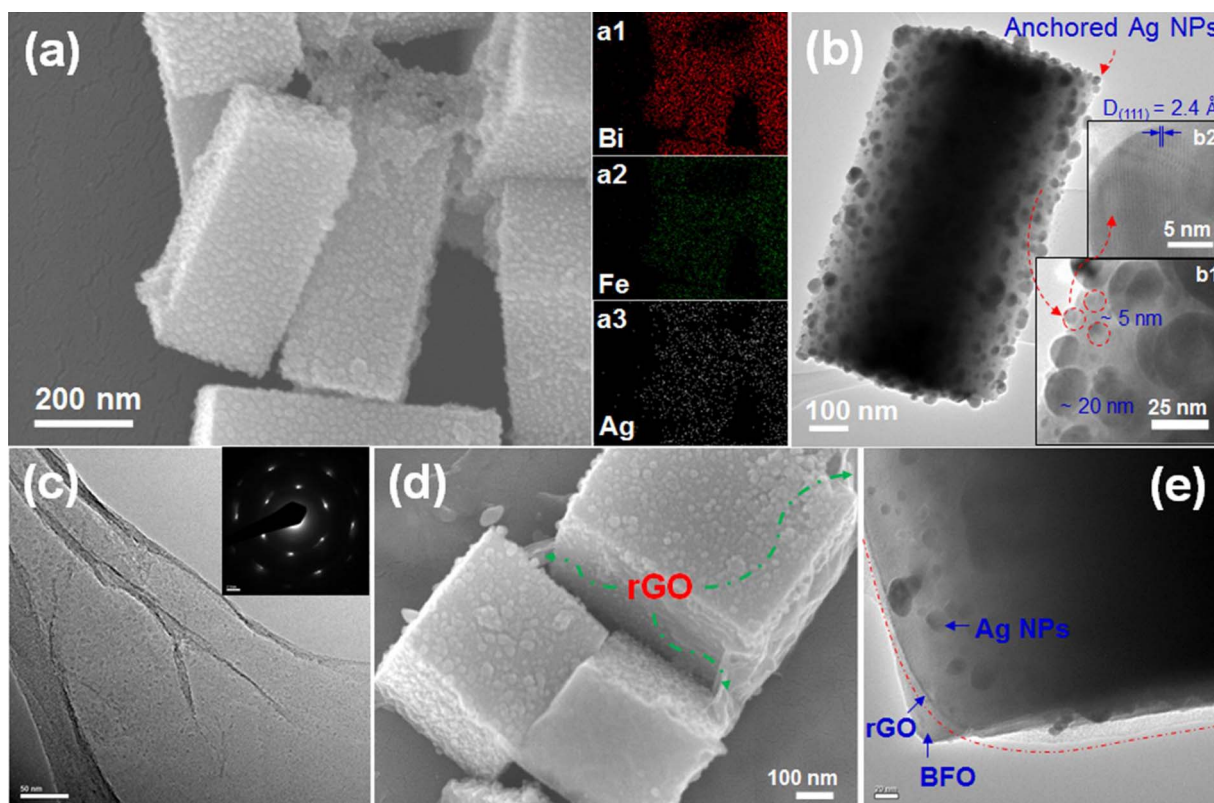
Fig. 2. (a) SEM image of Ag-decorated bismuth ferrite (BFOA1) and the corresponding EDX elemental distribution mapping of Bi (a1), Fe (a2) and Ag (a3) within BFOA1. (b) TEM image of BFOA1 and HRTEM image of Ag nanoparticles (b1, b2). (c) TEM image and the corresponding SAED pattern (inset) of rGO. (d) SEM image of BFOA1 with rGO wrapping (BFOA1-G). (e) TEM image of BFOA1-G.

These results demonstrate successful synthesis of the 0D-3D Ag-BFO nanostructured composites. Furthermore, the thickness of the exfoliated rGO sheet, which has a two-dimensional structure with wrinkles and curls (Fig. 2c), is estimated to be about 1.1 nm (Fig. S2) by atomic force microscope (AFM, Park System XE-100). The corresponding HRTEM within wrinkled area shows clear lattice fringes (Fig. S1e). The rGO can be well-dispersed in water with a light black color (Fig. 1) and the selected area electron diffraction (SAED) pattern (inset of Fig. 2c) verifies its hexagonal lattice structure. As shown in Fig. 2d, BFOA1 has been successfully wrapped by rGO. This 0D-2D-3D rGO-Ag/BFO nanostructured composite was further confirmed in TEM image, as shown in Fig. 2e, wherein BFOA1 is covered by a translucent rGO sheet. In addition, suspensions of BFO, BFOA1, BFOA5 and BFOA1-G are shown in Supporting Information (Fig. S1f). As can be seen, the color of suspensions is different among the as-prepared samples. Such evidence-based phenomenon reflects the difference in characteristics and properties of the synthesized BFO-based nanomaterials.

XRD was used to evaluate the crystalline phase of the as-prepared samples. As shown in Fig. 3a, the diffraction peaks of the nanocomposites (*i.e.*, BFOA1, BFOA5 and BFOA1-G) are consistent with those of pure BFO sample ($Bi_2F_4O_9$, JCPDS no. 04-009-6352) [34]. The characteristic peak of AgNPs cannot be observed in the pattern of BFOA1 owing to the lower fraction of AgNPs. With the increase in the amount of AgNPs (BFOA5), the major diffraction peak of AgNPs could be detected at 2θ of 38.2° assigned to plane (111) [33]. This result is consistent with the HRTEM result obtained above. There is no observable characteristic diffraction peak of rGO in the XRD pattern of BFOA1-G, indicating rGO maintain one- (or several-) layered structure without stacking among each other within the nanocomposites [31,35]. Moreover, XPS was used to investigate the chemical compositions and chemical binding states within the as-prepared samples. According to the binding energy (BE) spectra shown in Fig. 3b, the characteristic

peaks were detected in the as-prepared nanocomposites. The spectra contain not only Ag 3p and Ag 3d from decorated materials, but also Bi 4p, Bi 4d, Bi 4f and Fe 2p from host materials, which further indicates that the AgNPs have been successfully decorated on the BFO. Meanwhile, GO displays two satellite peaks at BE of 286.8 and 284.6 eV (Fig. 3b), which is assigned to C−O and C−C bonds. As compared with BFO and BFOA1, BFOA1-G also displays C 1s BE peaks at 285.79 eV with a slight shift accordingly. This evidence reflects the possible formation of chemical bonding between BFOA and rGO such as Bi−O−C and Fe−O−C bonds [28,36].

In the FT-IR transmittance spectra (Fig. 3c) of the as-prepared samples, the peaks at 3420 and 1630 cm^{-1} are assigned to −OH stretching vibration and H−O−H bending vibration of the adsorbed H_2O, respectively. The vibrational modes of oxygen − [transition metal ions] (v(M−O)) of all the samples, detected in the 400–900 cm^{-1} region, are very similar involving stretching modes of Fe−O and Bi−O, and bending modes of Fe−O−Fe and O−Fe−O within the related polyhedrons in BFO [31,37]. It is worth noticing that numerous characteristic peaks appeared in BFOA1 and BFOA5 compared to BFO, which may be attributed to the decorated AgNPs [38,39]. Another notable feature in the FT-IR spectrum of BFOA1-G is the additional characteristic peaks detected in the 1000–1800 cm^{-1} region, which can be assigned to the vibrational modes of GO (*i.e.*, v(GO)) including C=O stretching mode at 1728 cm^{-1}, C=C skeletal vibration at 1610 cm^{-1}, carboxyl C−OH stretching mode at 1383 cm^{-1}, phenolic C−OH stretching mode at 1225 cm^{-1} and C−O stretching mode at 1051 cm^{-1}. This finding is well consistent with our previous report [31], suggesting that BFOA1-G nanocomposite has been successfully fabricated. In addition, the TGA curves (Fig. S3) reveal that the experimental loading of rGO is ~ 4.5% by weight (the theoretical mass fraction of GO is 4.8%), indicating the experiments were conducted under good control. Furthermore, the UV–vis absorption spectrum of BFO (Fig. 3d) reveals that
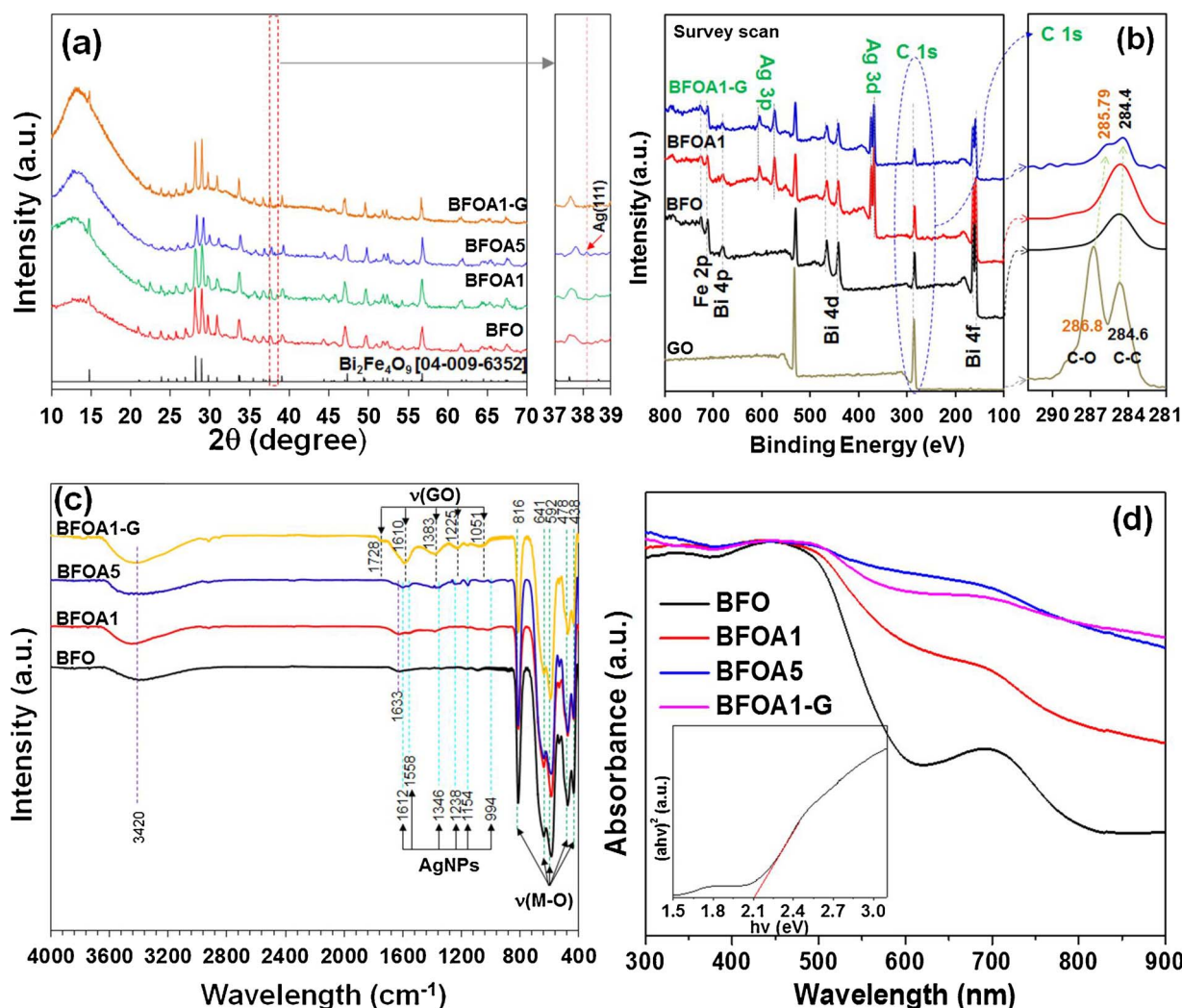
Fig. 3. (a) XRD patterns of BFO, BFOA1, BFOA5 and BFOA1-G. (b) XPS survey spectra of GO, BFO, BFOA1 and BFOA1-G, and the corresponding high resolution XPS spectra of C 1s. (c) FT-IR transmittance spectra of BFO, BFOA1, BFOA5 and BFOA1-G in the 400–4000 cm^{-1}. (d) UV–vis absorption spectra of BFO, BFOA1, BFOA5 and BFOA1-G, and the Kubelka-Munk transformed reflectance spectrum of BFO (inset).

BFO has a good light harvesting capability within visible light region with a narrow bandgap of 2.1 eV (Fig. 3d, inset), suggesting that BFO could be as a catalyst for visible light assisted catalysis. The light harvesting capability of BFO can be gradually enhanced with increase in AgNPs loading (Fig. 3d), which is contributed by the surface plasmon resonance (SPR) property of AgNPs [7]. Moreover, rGO also can be used to enhance light harvesting efficiency of BFOA1-G (Fig. 3d) [28,31]. It is anticipated to improve the disinfection efficacy due to an elaborative design in unique nanostructures.

3.2. Disinfection efficacy

In the research of nanocomposites for developing novel water disinfection technologies, it is vital to understand the following aspects: (1) functions (and/or influences) of the component materials within a nanocomposite, (2) potential disinfection systems driven by a nanocomposite, and (3) integrated performance of a nanocomposite on bactericidal efficiency. According to a series of designed experiments, comparative studies were conducted and plausible mechanisms were proposed by investigating the bactericidal activities of the as-prepared nanocomposites.

The viability of *E. coli* remains intact under controlled experimental conditions in dark while BFO did not deactivate bacteria (Fig. 4a), implying that BFO is nontoxic towards bacteria. However, BFOA

nanocomposites exhibited significant disinfection efficiency towards bacteria as proven by the reduction of the number of colony to nearly zero, as shown in Fig. 4a, wherein BFOA5 with increased AgNPs loading showed a higher bactericidal performance than BFOA1. It is ascribed to the antibacterial property of AgNPs as reported widely [5,6,40]. Since the controlled experiment conducted in the dark did not involve catalysis (dark/BFO system), the results are attributed to the following bactericidal mechanisms: (1) interruption of intracellular metabolic pathways through Ag$^+$ penetration into the cells (*e.g.*, inhibiting adenosine triphosphate formation and enzymes activity) [8–10,14,15]; and (2) physical damage of cell membrane by AgNPs owing to direct contact of the interface of BFOA with bacterial cells [13,41]. According to Ag$^+$ leaching test for BFOA (Table 1) and nearly zero colonies on agar plate with 6 logs of bacterial reduction (Fig. 4a and b, inset), the mechanism (1) is proposed in this study since physical damage with high randomness is unlikely to approach 100% bactericidal efficiency [8]. Moreover, Ag$^+$ released from BFOA1-G is extremely low (8.9 µg L^{-1}) at an estimated BFOA dosage of 760 µg L^{-1}. This indicates that rGO can effectively suppress Ag$^+$ leaching owing to its remarkable adsorption property [24], leading to a weaker disinfection efficacy of BFOA1-G than that of BFOA1 (Fig. 4b). These results provide evidence that BFOA and BFOA-G have bactericidal performances by utilizing the antibacterial property of the decorated AgNPs in dark/material system.

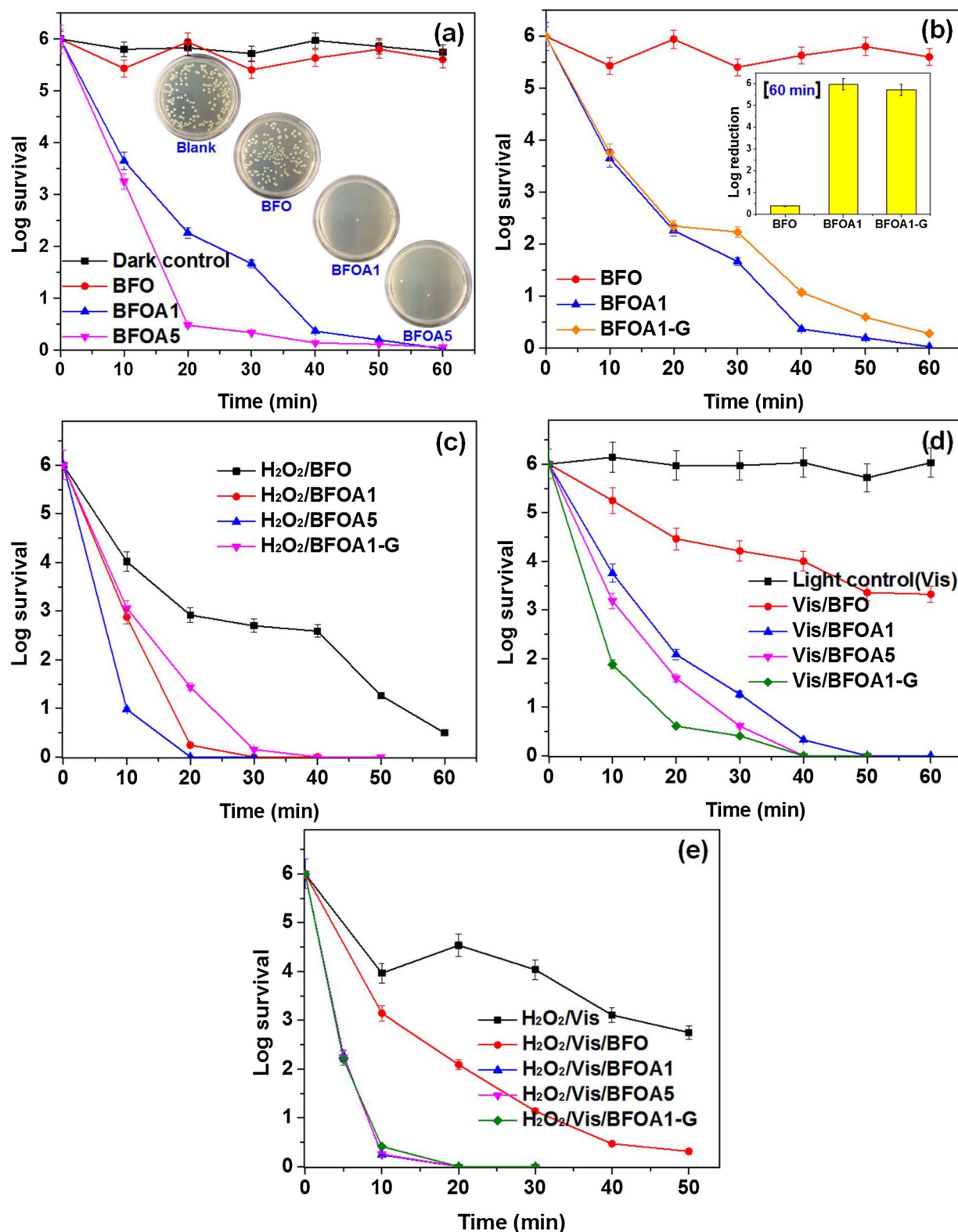Like the traditional technologies such as ozonation and

Fig. 4. (a) Comparison of the disinfection efficacies of BFO, BFOA1 and BFOA5 *via* contact with *E. coli* cells in Dark/material system; the inset shows the corresponding colony number of *E. coli* in 60 min. (b) Comparison of the disinfection efficacies of BFOA1 and BFOA1-G *via* contact with *E. coli* cells in Dark/material system; the inset shows the corresponding log reduction of *E. coli* in 60 min. Comparison of the disinfection efficacies of the as-prepared nanomaterials on *E. coli* cells in H_2O_2/material system (c), Vis/material system (d), and H_2O_2/Vis/material system (e).

chlorination, hydrogen peroxide (H_2O_2) as a strong oxidant can be used as antibacterial chemical but without the formation of harmful disinfection by-products (DBPs) [2,18]. However, the antibacterial efficacy was low along with high minimal bactericidal concentration (MBC,
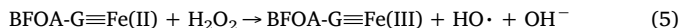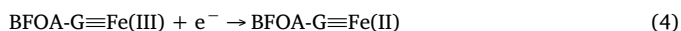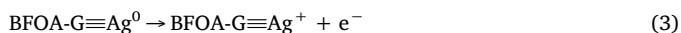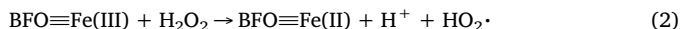
250 mg L^{-1}) (Fig. S4). Nevertheless, it could be effectively enhanced by using BFO as a peroxidase-like catalyst to activate a catalytic process (namely Fenton/Fenton-like reaction in H_2O_2/BFO system) with formation of HO$_2$· (Reaction (2)) [31,42]. As shown in Fig. 4c, H_2O_2/BFO

Table 1
Ag$^+$ released when the synthesized nanocomposites used in experimental systems.

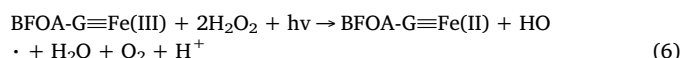| Nanocomposites	Ag$^+$ released (µg L^{-1})[a]			
	Dark/material	H$_2$O$_2$/material	Vis/material	H$_2$O$_2$/Vis/material
BFO	–	–	–	–
BFOA1	539	612	99	259
BFOA5	763	779	120	520
BFOA1-G	8.9	237	10.8	176

[a] Ag$^+$ leaching measurement using ICP-MS.

system in dark could deactivate over 5 logs of viable bacteria under the conditions of 0.1 g L^{-1} BFO, 60 mg L^{-1} H$_2$O$_2$ and 0.01 M PBS. The effect of operating factors (*e.g.*, H$_2$O$_2$ dosage and BFO loading) on disinfection efficacies were investigated as well (Figs. S5 and S6), showing that disinfection efficacy in this system increases with the increase of catalyst loading and chemical dosage. Additionally, H$_2$O$_2$/nanocomposite (*i.e.*, BFOA, BFOA-G) system exhibited significantly higher disinfection efficacy (100% in 30–40 min) than that of dark/nanocomposite system (~100% in 60 min) (Fig. 4c) as expected owing to the synergism of Fenton/Fenton-like reaction and antibacterial property of AgNPs. The additional mechanism for inactivation of bacteria within H$_2$O$_2$/nanocomposite system is the formation of ROSs by AgNPs assisted Fenton reaction (Reactions (3)–(5)) with conversion of H$_2$O$_2$ to HO· [28,43], which led to accelerate Ag$^+$ leaching (as shown in Table 1) and generate Fe^{2+} state within BFO (as detected by XPS in our previous report) [28].

$$BFO \equiv Fe(III) + H_2O_2 \rightarrow BFO \equiv Fe(II) + H^+ + HO_2· \tag{2}$$

$$BFOA\text{-}G \equiv Ag^0 \rightarrow BFOA\text{-}G \equiv Ag^+ + e^- \tag{3}$$

$$BFOA\text{-}G \equiv Fe(III) + e^- \rightarrow BFOA\text{-}G \equiv Fe(II) \tag{4}$$

$$BFOA\text{-}G \equiv Fe(II) + H_2O_2 \rightarrow BFOA\text{-}G \equiv Fe(III) + HO· + OH^- \tag{5}$$

Unlike UV radiation, visible light (420–630 nm) irradiation could not deactivate bacteria (Fig. 4d). Meanwhile, BFO-driven photocatalytic disinfection exhibited a weak bacterial deactivation (> 2.5 logs) in 60 min, which is possibly due to high recombination of e$^-$/h$^+$ pairs and less formation of O$_2$·$^-$ [20,31]. On the contrary, BFOA and BFOA1-G showed significant disinfection efficacy in the order of BFOA1-G > BFOA5 > BFOA1. In Vis/BFOA system, it is worth noting that this system was not accelerated by a potential synergistic action between AgNPs and BFO because AgNPs only can conduct photogenerated electrons but cannot effectively suppress the recombination of e$^-$/h$^+$ pairs [28]. These phenomena can be evidenced by the achieved results in photocatalytic degradation (Fig. S7).

and photoluminescence spectra (Fig. S8). Otherwise, AgNPs in Vis/BFOA system might slow down disinfection processes (Fig. S9) *via* competitive consumption of photogenerated electrons, which can lead to reduction of Ag$^+$ leaching (Table 1). Therefore, rGO plays the most important role in photocatalytic disinfection in Vis/BFOA-G system through successful inhibition of recombination of e$^-$/h$^+$ pairs and AgNPs are used to transfer electrons contributed by the good conductivity.

As compared to above systems, the as-prepared samples in H$_2$O$_2$/Vis/material system showed the best disinfection efficacy (Fig. 4e). In particular, H$_2$O$_2$/Vis/nanocomposite systems exhibited ultra-effective disinfection efficacy reaching 100% in 20 min. Irradiating BFOA1-G by visible light with the presence of H$_2$O$_2$, photo-Fenton oxidation involving formation of HO· can be excited based on Reaction (6). This is beneficial for the generation of Fe^{2+} state within BFOA-G composites followed by excited Fenton reaction (Reaction (5)) as demonstrated in the previous reported [31,42].

$$BFOA\text{-}G \equiv Fe(III) + 2H_2O_2 + hv \rightarrow BFOA\text{-}G \equiv Fe(II) + HO· + H_2O + O_2 + H^+ \tag{6}$$

Moreover, AgNPs assisted Fenton reaction (Reactions (3)–(5)) can be effectively accelerated as a result of surface plasmon resonance (SPR) of AgNPs when absorbing visible light [7,28]. Besides these two mechanisms (denoted as AgNPs assisted photo-Fenton), there are simultaneous mechanisms mentioned above including rGO assisted Ag$^+$ released, AgNPs assisted Fenton reaction and rGO/Ag co-assisted photocatalysis synergized within H$_2$O$_2$/Vis/BFO-G system. Hence, H$_2$O$_2$/Vis/BFOA-G system showed remarkable bactericidal performance, as well as degradation efficiency (Fig. S10). Fig. 5a shows a summary of disinfection efficacies of the as-prepared samples in different experimental systems in 20 min. It is obvious that both 0D-3D BFOA1 and 0D-2D-3D BFOA1-G nanocomposites exhibit excellent bactericidal performance reaching 6 logs of bacterial reduction with no living colony (*i.e.*, 100% efficacy). Nevertheless, 0D-2D-3D BFOA1-G nanocomposite is the more ideal option because it shows better disinfection in Vis/material system with a low-level release of Ag$^+$ (Table 1), *i.e.*, a greener and more sustainable technology. Moreover, Fig. 5b1 evidenced the integrity of the bacterial cell membranes before disinfection experiments, whereas all of the cell membranes were damaged after experiments (Fig. 5b2) (original images shown in Figs. S11 and S12) due to the formation of ROSs rather than physical puncturing of the cell walls by BFOA1-G [8]; confirming further that H$_2$O$_2$/Vis/BFOA1-G system can be an ultra-effective "integrated technology" for water disinfection. Besides *E. coli*, this system is also effective in inactivating other types of bacteria such as *P. aeruginosa* and *S. aureus* (Fig. 5c2 and d2). Furthermore, BFOA1-G has a good reusability as indicated by the log reduction values over three cycles of operation (Fig. S13).
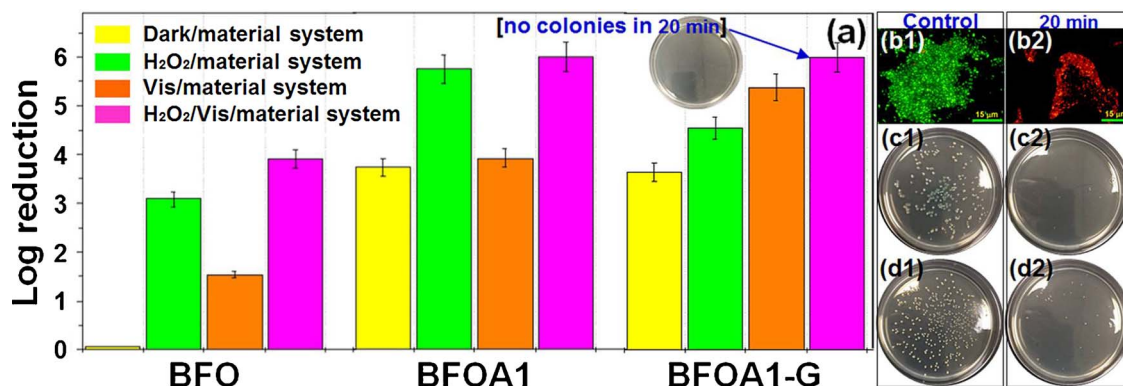

Fig. 5. (a) Disinfection efficacies of the as-prepared nanomaterials on *E. coli* in 20 min in different systems; the inset shows no colonies observed after disinfection *via* an integrated H$_2$O$_2$/Vis/BFOA1-G system. Fluorescence images (recorded using dual color channels) of *E. coli* cells before (b1) and after (b2) disinfection *via* H$_2$O$_2$/Vis/BFOA1-G system. Colony number of *P. aeruginosa* (c1, c2) and *S. aureus* (d1, d2) before and after (20 min) disinfection *via* H$_2$O$_2$/Vis/BFOA1-G system.
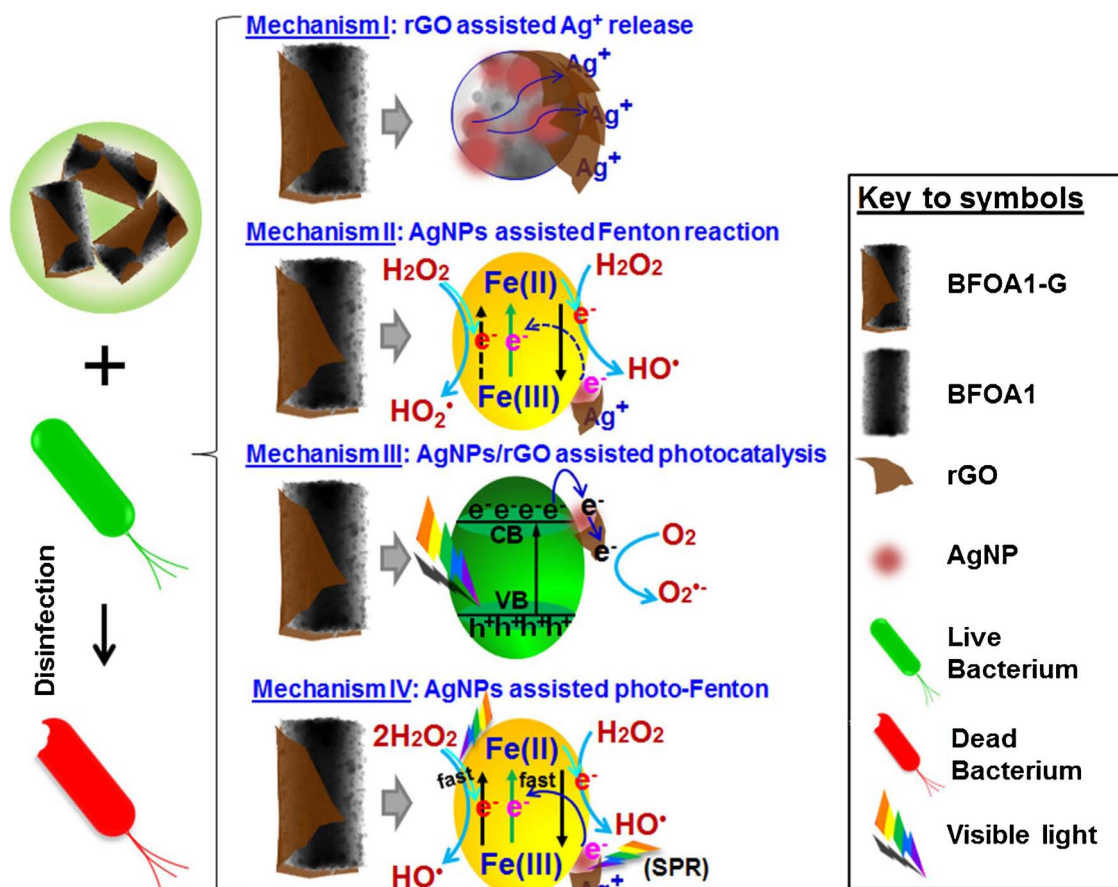
Fig. 6. Illustration summarizing the proposed bactericidal mechanisms (I–IV) in H_2O_2/Vis/BFOA1-G system.

Based on above-mentioned results, Fig. 6 summarizes the proposed bactericidal mechanisms in H_2O_2/Vis/BFOA1-G system including rGO assisted Ag^+ release, Ag assisted Fenton reaction, Ag/rGO assisted photocatalysis and Ag assisted photo-Fenton oxidation. Through oxidative dissolution of AgNPs, Ag^+ ions can be released and adhered on the surface of BFOA1-G by virtue of adsorption properties of rGO. The Ag^+ can penetrate cell membrane when contacting with bacteria (Mechanism I). The electrons (e^-) released during the conversion of Ag/Ag^+ can be used to promote the interconversion from Fe^{3+} to Fe^{2+} states within BFO (green line with arrow shown in Mechanism II) followed by excited Fenton reaction with the consumption of auxiliary H_2O_2 and the formation of HO·. The rate-limiting step of Fenton-like process (dashed line with arrow) in the redox cycle of Fe^{3+}/Fe^{2+} pair [44] can be replaced and/or assisted by the decorated AgNPs. Under visible light irradiation without H_2O_2, the photogenerated e^- can be transferred to conductive AgNPs followed by rGO effectively. It inhibits recombination of e^-/h^+ pairs and enhances formation of O_2·$^-$ (Mechanism III). If there are co-existing auxiliary H_2O_2 during photocatalysis, photo-Fenton oxidation can be activated to replace the rate-limiting step (solid line with arrow shown in mechanism IV). Meanwhile, the conversion of Ag/Ag^+ can be accelerated due to the surface plasmon resonance (SPR). Therefore, the interconversion speed from Fe^{3+} to Fe^{2+} states within BFO is redoubled followed by enhanced formation of HO· in AgNPs assisted photo-Fenton oxidation. As a comparison, a summary of the bactericidal mechanisms of the resultant samples (*e.g.,* three types of BFOA-G, BFOA and BFO) is shown in Table S1. Moreover, HO· was successfully detected with the terephthalic acid solution using the fluorescence technique in H_2O_2/Vis/BFOA1-G system (Fig. S14) [45]. As compared with untreated *E. Coli* cells (Fig. S14b), the cell-membrane damage was obvious when exposed cells in H_2O_2/ Vis/BFOA1-G system (Fig. S14c). This phenomenon implies that

bacterial inactivation is likely caused by ROSs generated in above designed system [8].

4. Conclusions

A novel 0D-2D-3D nanostructured rGO-Ag/BFO composite (BFOA-G) has been designed and produced by incorporating 2D rGO into the *in-situ* synthesized 0D-3D Ag-BFO nanocomposite *via* a facile evaporation process under mild conditions. A novel bactericidal technology which integrates multiple water disinfection technologies in BFOA-G composite based H_2O_2/Vis/BFOA-G system is elucidated and demonstrated. In this study, BFOA-G exhibited ultra-effective bactericidal performance (~100% efficacy within 20 min) with the inhibition of Ag^+ leaching, which is contributed to the synergism among the component materials within nanostructured composites. The findings highlight the potential of employing that multi-phase nanostructured composite for developing an "integrated technology" of water disinfection associated with the concept of enhanced bactericidal efficacy while ensuring environmental-friendliness and sustainability.

Appendix A. Supplementary data

Supplementary data associated with this article can be found, in the online version, at https://doi.org/10.1016/j.apcatb.2018.01.047.

References

[1] W.H. Organization, Progress on Sanitation and Drinking Water: 2015 Update and MDG Assessment, World Health Organization, 2015.

[2] D.L. Sedlak, U. von Gunten, The chlorine dilemma, Science 331 (2011) 42–43.

[3] W. Hijnen, E. Beerendonk, G.J. Medema, Inactivation credit of UV radiation for viruses, bacteria and protozoan (oo) cysts in water: a review, Water Res. 40 (2006) 3–22.

[4] D.M. Morens, A.S. Fauci, Emerging infectious diseases: threats to human health and global stability, PLoS Pathog. 9 (2013) e1003467.

[5] M. Rai, A. Yadav, A. Gade, Silver nanoparticles as a new generation of anti-microbials, Biotechnol. Adv. 27 (2009) 76–83.

[6] L. Rizzello, P.P. Pompa, Nanosilver-based antibacterial drugs and devices: mechanisms, methodological drawbacks, and guidelines, Chem. Soc. Rev. 43 (2014) 1501–1518.

[7] K. Awazu, M. Fujimaki, C. Rockstuhl, J. Tominaga, H. Murakami, Y. Ohki, N. Yoshida, T. Watanabe, A plasmonic photocatalyst consisting of silver nanoparticles embedded in titanium dioxide, J. Am. Chem. Soc. 130 (2008) 1676–1680.

[8] S.-L. Loo, W.B. Krantz, A.G. Fane, Y. Gao, T.-T. Lim, X. Hu, Bactericidal mechanisms revealed for rapid water disinfection by superabsorbent cryogels decorated with silver nanoparticles, Environ. Sci. Technol. 49 (2015) 2310–2318.

[9] P. Dibrov, J. Dzioba, K.K. Gosink, C.C. Häse, Chemiosmotic mechanism of antimicrobial activity of Ag+ in Vibrio cholerae, Antimicrob. Agents Chemother. 46 (2002) 2668–2670.

[10] H.-J. Park, J.Y. Kim, J. Kim, J.-H. Lee, J.-S. Hahn, M.B. Gu, J. Yoon, Silver-ion-mediated reactive oxygen species generation affecting bactericidal activity, Water Res. 43 (2009) 1027–1032.

[11] L. Maurer, J. Meyer, A systematic review of evidence for silver nanoparticle-induced mitochondrial toxicity, Environ. Sci. Nano 3 (2016) 311–322.

[12] J. Fabrega, S.N. Luoma, C.R. Tyler, T.S. Galloway, J.R. Lead, Silver nanoparticles: behaviour and effects in the aquatic environment, Environ. Int. 37 (2011) 517–531.

[13] S.-L. Loo, A.G. Fane, T.-T. Lim, W.B. Krantz, Y.-N. Liang, X. Liu, X. Hu, Superabsorbent cryogels decorated with silver nanoparticles as a novel water technology for point-of-use disinfection, Environ. Sci. Technol. 47 (2013) 9363–9371.

[14] X. Wang, H. Dong, Q. Zeng, Q. Xia, L. Zhang, Z. Zhou, Reduced iron-containing clay minerals as antibacterial agents, Environ. Sci. Technol. 51 (2017) 7639–7647.

[15] P.V.L. Reddy, B. Kavitha, P.A.K. Reddy, K.-H. Kim, TiO2-based photocatalytic disinfection of microbes in aqueous media: a review, Environ. Res. 154 (2017) 296–303.

[16] Z. Wang, B. Mi, Environmental applications of 2D molybdenum disulfide (MoS2) nanosheets, Environ. Sci. Technol. (2017).

[17] R.A. Pizarro, L.V. Orce, Membrane damage and recovery associated with growth delay induced by near-UV radiation in Escherichia coli K-12, Photochem. Photobiol. 47 (1988) 391–397.

[18] K. Song, M. Mohseni, F. Taghipour, Application of ultraviolet light-emitting diodes (UV-LEDs) for water disinfection: a review, Water Res. 94 (2016) 341–349.

[19] Z.G. Zhao, M. Miyauchi, Nanoporous-walled tungsten oxide nanotubes as highly active visible-light-driven photocatalysts, Angew. Chem. 120 (2008) 7159–7163.

[20] M.D. Hernández-Alonso, F. Fresno, S. Suárez, J.M. Coronado, Development of alternative photocatalysts to TiO2: challenges and opportunities, Energy Environ. Sci. 2 (2009) 1231–1257.

[21] H. Zhang, G. Chen, Potent antibacterial activities of Ag/TiO2 nanocomposite powders synthesized by a one-pot sol- gel method, Environ. Sci. Technol. 43 (2009) 2905–2910.

[22] C. An, S. Peng, Y. Sun, Facile synthesis of sunlight-driven AgCl:Ag plasmonic nanophotocatalyst, Adv. Mater. 22 (2010) 2570–2574.

[23] X. Wang, T.-T. Lim, Highly efficient and stable Ag-AgBr/TiO2 composites for destruction of Escherichia coli under visible light irradiation, Water Res. 47 (2013) 4148–4158.

[24] B.F. Machado, P. Serp, Graphene-based materials for catalysis, Catal. Sci. Technol. 2 (2012) 54–75.

[25] M. Huang, J. Yu, Q. Hu, W. Su, M. Fan, B. Li, L. Dong, Preparation and enhanced photocatalytic activity of carbon nitride/titania (001 vs 101 facets)/reduced graphene oxide (gC3N4/TiO2/rGO) hybrids under visible light, Appl. Surf. Sci. 389 (2016) 1084–1093.

[26] X. Zeng, Z. Wang, G. Wang, T.R. Gengenbach, D.T. McCarthy, A. Deletic, J. Yu, X. Zhang, Highly dispersed TiO2 nanocrystals and WO3 nanorods on reduced graphene oxide: Z-scheme photocatalysis system for accelerated photocatalytic water disinfection, Appl. Catal. B: Environ. 218 (2017) 163–173.

[27] H. Zhang, L.-H. Guo, D. Wang, L. Zhao, B. Wan, Light-induced efficient molecular oxygen activation on a Cu (Ii)-grafted TiO2/graphene photocatalyst for phenol degradation, ACS Appl. Mater. Interfaces 7 (2015) 1816–1823.

[28] Z.-T. Hu, S.K. Lua, T.-T. Lim, Cuboid-like Bi2Fe4O9/Ag with graphene-wrapping tribrid composite with superior capability for environmental decontamination: nanoscaled material design and visible-light-driven multifunctional catalyst, ACS Sustain. Chem. Eng. 3 (2015) 2726–2736.

[29] Z.-T. Hu, S.K. Lua, X. Yan, T.-T. Lim, Nanostructured hexahedron of bismuth ferrite clusters: delicate synthesis processes and an efficient multiplex catalyst for organic pollutant degradation, RSC Adv. 5 (2015) 86891–86900.

[30] W. Humers, R. Offeman, Preparation of graphitic oxide, J. Am. Chem. Soc. 80 (1958) 1339.

[31] Z.-T. Hu, J. Liu, X. Yan, W.-D. Oh, T.-T. Lim, Low-temperature synthesis of graphene/Bi2Fe4O9 composite for synergistic adsorption-photocatalytic degradation of hydrophobic pollutant under solar irradiation, Chem. Eng. J. 262 (2015) 1022–1032.

[32] G. Grégori, S. Citterio, A. Ghiani, M. Labra, S. Sgorbati, S. Brown, M. Denis, Resolution of viable and membrane-compromised bacteria in freshwater and marine waters based on analytical flow cytometry and nucleic acid double staining, Appl. Environ. Microbiol. 67 (2001) 4662–4670.

[33] J. Keuler, L. Lorenzen, R. Sanderson, V. Prozesky, W. Przybylowicz, Characterization of electroless plated palladium-silver alloy membranes, Thin Solid Films 347 (1999) 91–98.

[34] E. Kostiner, G.L. Shoemaker, Mössbauer effect study of Bi2Fe4O9, J. Solid State Chem. 3 (1971) 186–189.

[35] D.A. Dikin, S. Stankovich, E.J. Zimney, R.D. Piner, G.H. Dommett, G. Evmenenko, S.T. Nguyen, R.S. Ruoff, Preparation and characterization of graphene oxide paper, Nature 448 (2007) 457.

[36] J. An, L. Zhu, N. Wang, Z. Song, Z. Yang, D. Du, H. Tang, Photo-Fenton like degradation of tetrabromobisphenol A with graphene BiFeO3 composite as a catalyst, Chem. Eng. J. 219 (2013) 225–237.

[37] M.M. Murshed, G. Nénert, M. Burianek, L. Robben, M. Mühlberg, H. Schneider, R.X. Fischer, T.M. Gesing, Temperature-dependent structural studies of mullite-type Bi2Fe4O9, J. Solid State Chem. 197 (2013) 370–378.

[38] R. Augustine, K. Rajarathinam, Synthesis and characterization of silver nanoparticles and its immobilization on alginate coated sutures for the prevention of surgical wound infections and the in vitro release studies, Int. J. Nano Dimens. 2 (2012) 205–212.

[39] W. Wrótniak-Drzewiecka, S. Gaikwad, D. Laskowski, H. Dahm, J. Niedojadło, A. Gade, M. Rai, Novel approach towards synthesis of silver nanoparticles from Myxococcus virescens and their lethality on pathogenic bacterial cells, Austin J. Biotechnol. Bioeng. 1 (2014) 7.

[40] S. Chernousova, M. Epple, Silver as antibacterial agent: ion, nanoparticle, and metal, Angew. Chem. Int. Ed. 52 (2013) 1636–1653.

[41] I. Sondi, B. Salopek-Sondi, Silver nanoparticles as antimicrobial agent: a case study on E. coli as a model for gram-negative bacteria, J. Colloid Interface Sci. 275 (2004) 177–182.

[42] Z.T. Hu, W.D. Oh, Y. Liu, E.H. Yang, T.T. Lim, Controllable mullite bismuth ferrite micro/nanostructures with multifarious catalytic activities for switchable/hybrid catalytic degradation processes, J. Colloid Interface Sci. 509 (2017) 502–514.

[43] X. Qian, M. Ren, Y. Zhu, D. Yue, Y. Han, J. Jia, Y. Zhao, Visible light assisted heterogeneous Fenton-like degradation of organic pollutant via α-FeOOH/mesoporous carbon composites, Environ. Sci. Technol. 51 (2017) 3993–4000.

[44] C. Walling, A. Goosen, Mechanism of the ferric ion catalyzed decomposition of hydrogen peroxide. Effect of organic substrates, J. Am. Chem. Soc. 95 (1973) 2987–2991.

[45] K.I. Ishibashi, A. Fujishima, T. Watanabe, K. Hashimoto, Detection of active oxidative species in TiO2 photocatalysis using the fluorescence technique, Electrochem. Commun. 2 (2000) 207–210.